Supporting Information for

Interconnected 3D carbon network with enhanced reaction kinetics and architecture stability for advanced potassium-ion hybrid capacitors

Fei Yuan [a, b], Di Zhang [b], Qiyao Yu [c], Zhaojin Li [b], Qiujun Wang [b], Huan Wang [b], Yusheng Wu [a, *],

Bo Wang [b, *]

[a] *School of Materials Science and Engineering, Shenyang University of Technology, Shenyang 110870, China*

[b] *Hebei Key Laboratory of Flexible Functional Materials, School of Materials Science and Engineering, Hebei University of Science and Technology, Shijiazhuang 050000, China*

[c] *State Key Laboratory of Explosion Science and Technology, School of Mechatronical Engineering, Beijing Institute of Technology, Beijing 100081, China*

*Corresponding authors.

E-mail addresses: lizhaojin1214@163.com (Z. L), wuyus@sut.edu.cn (Y. W),

wangbo1996@gmail.com (B. W).

Experimental section

Synthesis of PC and NPC: PC was prepared by direct carbonization of sodium citrate at 750 °C for 3 h under inert atmosphere with a temperature ramp rate of 2 °C min^{-1}. The as-obtained dark product was then washed with deionized water, and absolute ethyl alcohol to remove the *in situ* generated template (sodium carbonate). Subsequently, the obtained product was dried in an oven at 70 °C for 10 h. The preparation of NPC was conducted according to the same procedure as PC except that the raw material was a mixture of sodium citrate and urea (mass ratio = 1: 2). The porous carbon control samples carbonized at different temperatures were denoted as PC-650 (650 °C) and PC-850 (850 °C). And the samples with different ratios of sodium citrate and urea (mass ratio = 1: 1 and 1: 2) were also prepared, and these obtained products were denoted as NPC-1 and NPC-3.

Materials Characterizations: The morphologies were investigated by scanning electron microscopy (SEM, Hitachi SU8010) and transmission electron microscopy (TEM, JEOL JEM-2010). The chemistry information was examined by XRD (Bruker D2 Phaser X-Ray Diffractometer with Cu Kα radiation) and Raman spectroscopy (a Kr-Ar ion laser at 633 nm produced by Spectra-Physics Beamlok 2060-RS laser combining Symphony CCD-1LS detection system). The nitrogen adsorption-desorption isotherms were measured with a Quantachrome Autosorb AS-6B system. The near surface chemical state of different elements was also done via X-ray photoelectron spectroscopy (XPS, ESCALAB 250 Xi).

Computational Methods： All the calculations were based on density functional theory by using the Vienna ab-initio simulation package (VASP). The generalized gradient approximation (GGA) with the function of Perdew-Becke-Ernzerhof (PBE) was employed to describe the electron interaction energy of exchange correlation. The projector augmented wave was applied to describe the electrion-ion interaction and the plane-wave energy cutoff was set to 400 eV. All structures were optimized with a convergence criterion of 1×10^{-5} eV for the energy and 0.01 eV/Å for the forces. Brillouin zone sampling was employed using a Monkhorst-Packing grid with 3×3×1. The K-embedding energy (ΔE)

is defined as the following Equation:

$$\Delta E=[E_2-(E_1+\mu K)]$$

where E_1 and E_2 are the total energies of the system before and after potassium embedding, respectively, and μK is the chemical potential of potassium bulk. A positive ΔE indicates an endothermic and unstable K insertion reaction while a negative ΔE suggests an exothermic and stable reaction.

Electrochemical Measurements: The working electrodes were composed of the as-obtained active material, acetylene black (AB) and polyvinylidene fluoride (PVDF) with a mass ratio of 7:2:1. The slurry was cast onto the aluminum foil and dried at 80 °C under vacuum for 10 h. The mass loading of the active material on the working electrodes was about 1.4 mg cm^{-2}. Coin cells (CR2032) were assembled with potassium foil as the counter/reference electrode, a glass-fiber separator, and 0.8 M KPF$_6$/EC/DEC (1:1 by volume ratio) as an electrolyte in argon-filled glove box. The galvanostatic tests of cycle and rate performance were tested by multi-channel land battery test system (LAND-CT2001A) in the fixed voltage window from 0.01 V to 2.5 V versus K$^+$/K at room temperature. Cyclic voltammetry (CV) was conducted by a Gamry electrochemical workstation with a scan rate of 0.1 mV s^{-1}. Electrochemical impedance spectroscopy (EIS) was measured on a Gamry electrochemical workstation over the frequency range from 0.01 to 10^5 Hz (amplification voltage: 5 mV). Besides, the potassium-ion hybrid capacitors (PIHCs) were assembled, which used the NPC and activated carbon (AC) as the anode and cathode, respectively, and used the same separator and electrolyte as those in potassium ion half-cell. Particularly, AC was purchased form Aladdin, and the BET specific surface area was 1800 m^2 g^{-1}. Before assembling the PIHCs, the anode and cathode were performed a pre-treatment process by charging and discharging a few times at a current density of 100 mA g^{-1} in a half-cell. In particular, the cathode electrode was prepared by mixing 90 *wt*% AC, 5 *wt*% AB and 5 *wt*%

PVDF. The mass loading of the AC cathode was approximately four times larger than that of the NPC anode. The potential range of AC and PIHCs was 2.0-4.0 V and 0.01-4.0 V, respectively. The energy densities (E) and power densities (P) of PIHCs were calculated by numerically integrating the galvanostatic discharge profiles using the equations below
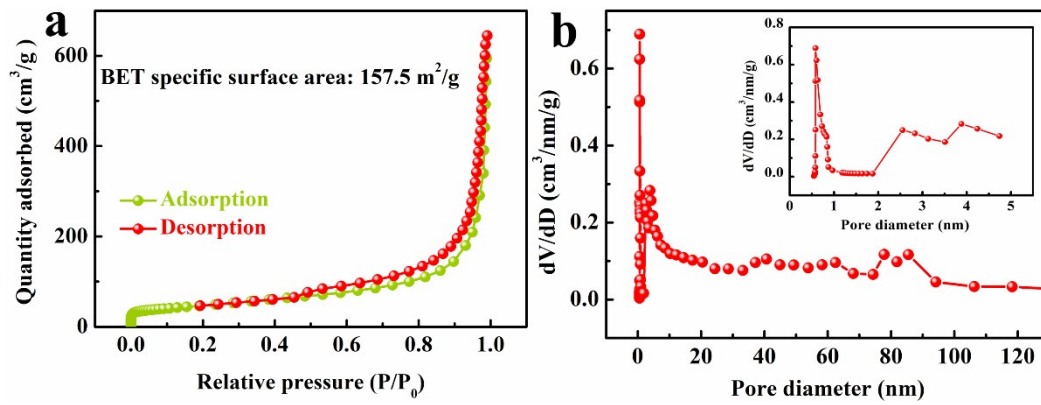
$$E = \int_{t1}^{t2} IVdt = \Delta V \times \frac{I}{m} \times t \qquad (1)$$
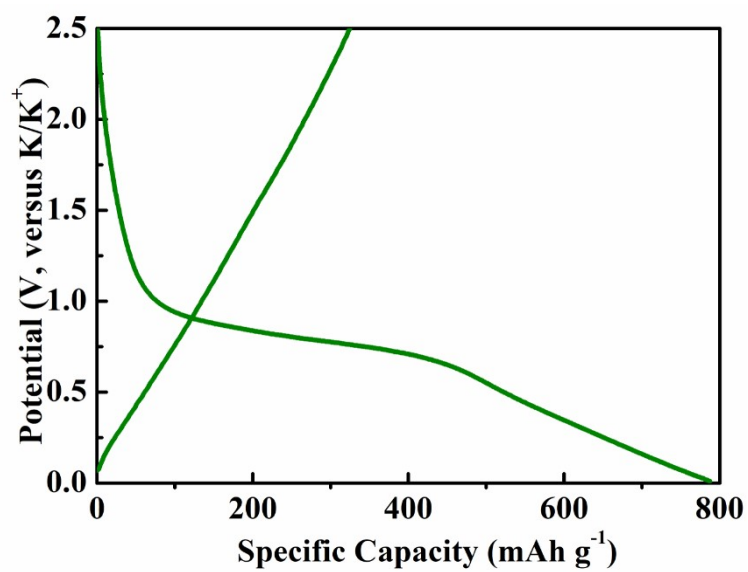
$$P = \frac{E}{t} \qquad (2)$$

where I was the charge/discharge current, V was the working voltage, t_1 and t_2 were the start/end-of-discharge time (s), respectively, and t corresponds to the discharge time.
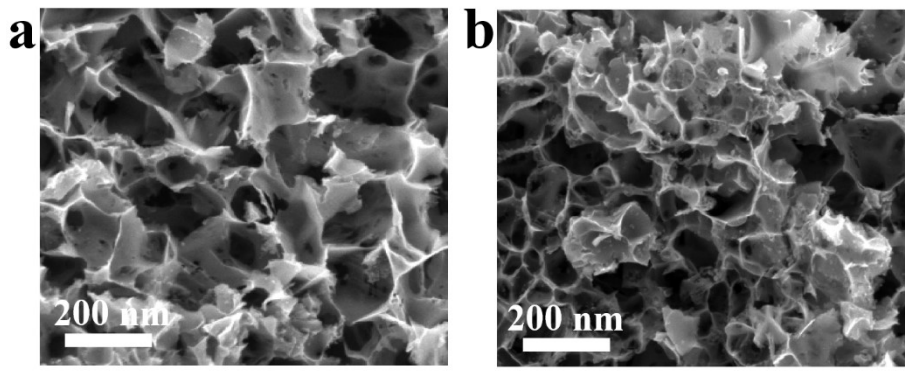
Figure S1. SEM images of PC.

Figure S2. Nitrogen adsorption-desorption isotherms (a) and pore size distribution (b) of PC.
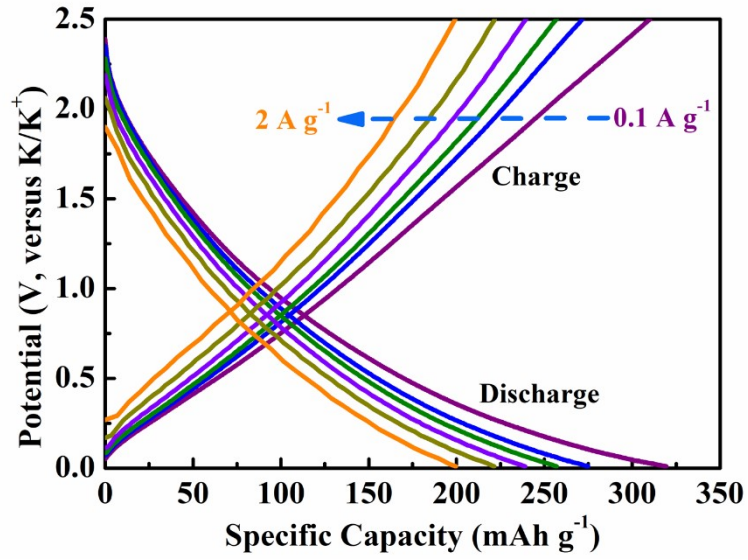
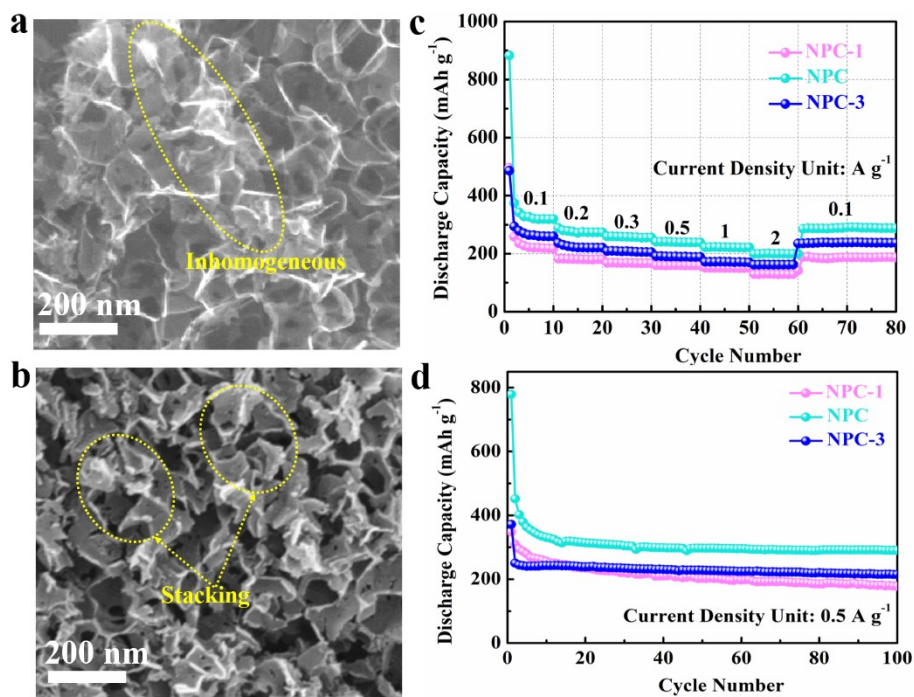**Figure S3.** The initial charge and discharge profiles of NPC at 0.5 A g^{-1}.
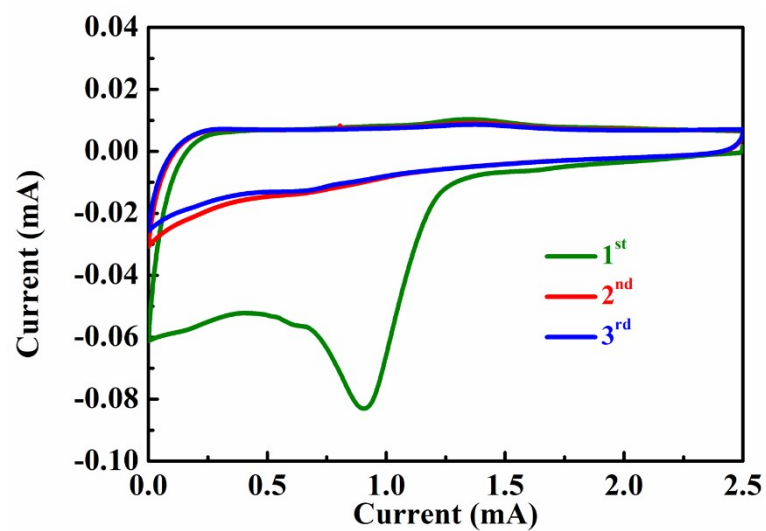
Figure S4. CV profiles of NPC at a scan rate of 0.1 mV s^{-1} between 0.01 and 2.5 V (*versus* K$^+$/K).

Figure S5. The charge and discharge profiles of NPC at various current densities of 0.1, 0.2, 0.3, 0.5,1 and

2 A g^{-1}.

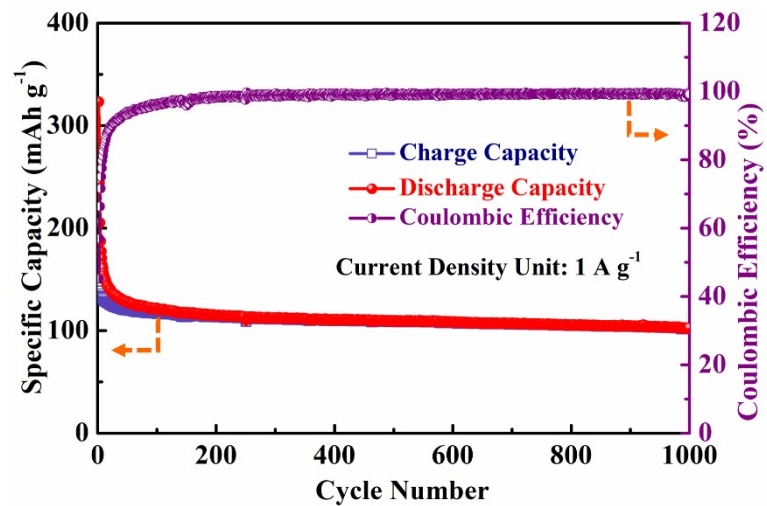**Figure S6.** SEM images of NPC-1 (a) and NPC-3 (b). (c) Rate and (d) cycling performance of NPC-1 and NPC-3.
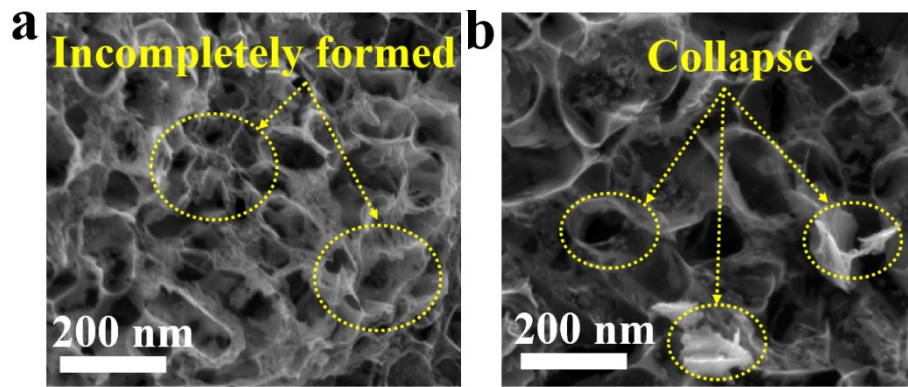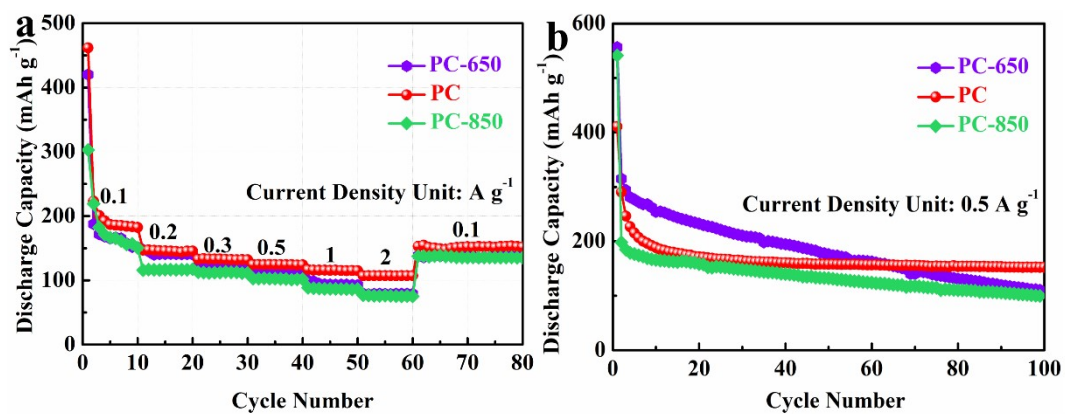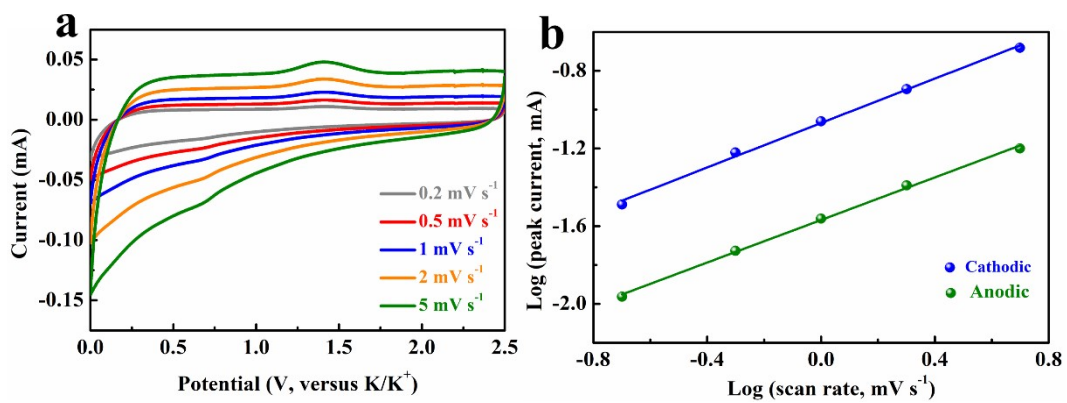
Figure S7. Cycle performance of PC at a high current density of 1 A g^{-1} for 1000 cycles.

Figure S8. SEM images of PC-650 (a) and PC-850 (b).

Figure S9. The electrochemical performance comparison of PC-650, PC and PC-850. (a) Rate capability.

(b) Cycling stability at current density of 0.5 A g^{-1} for 100 cycles.

Figure S10. (a) CV curves at different scan rates from 0.2 to 5 mV s^{-1}, (b) *b*-value analysis using the relationship between the peak currents and the scan rates in CV curves of PC.
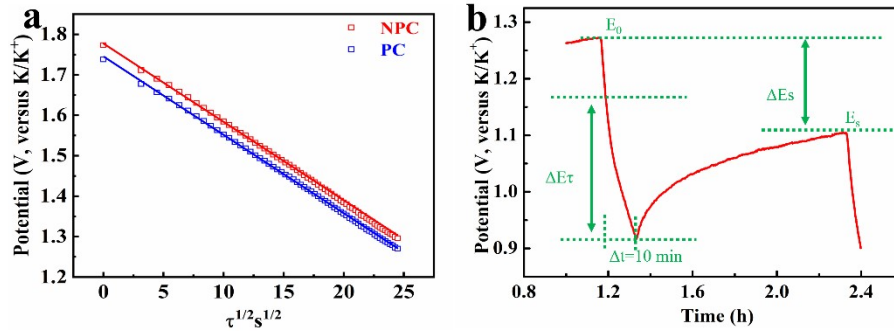
Figure S11. (a) Linear behavior of the potential *vs*. $\tau^{1/2}$. (b) Schematic of the calculation of diffusion coefficient using GITT technique.

The ionic diffusion coefficient in PC and NPC electrodes can be determined by solving Fick's second law with the following equation[1]

$$D = \frac{4}{\pi\tau}\left(\frac{m_B V_M}{M_B S}\right)^2 \left(\frac{\Delta E_s}{\tau\left(\frac{dE_\tau}{d\sqrt{\tau}}\right)}\right)^2 \qquad (\tau << \frac{L^2}{D}) \qquad (1)$$

where m_B is electrode active mass; M_B is the molar mass of the electrode material for carbon; V_M is the molar volume of hard carbon; S is the geometric area of the electrode; M_B/V_M is obtained from the density of NPC and NC, L is the average thickness of the electrode. If the cell potential is linearly proportional to $\tau^{1/2}$ Figure S11a, Equation (1) can be further simplified to
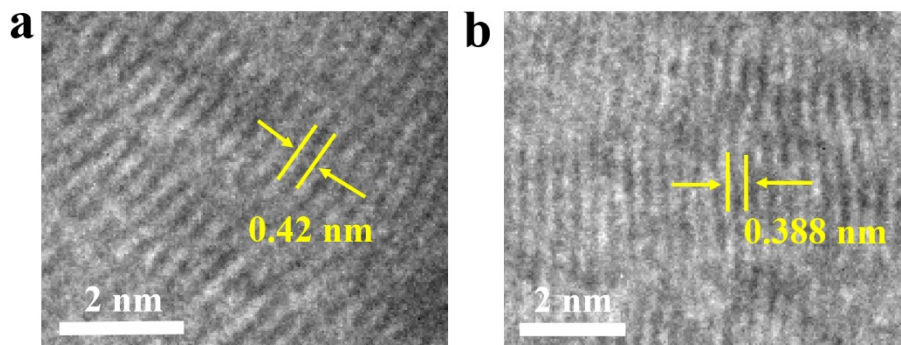
$$D = \frac{4}{\pi\tau}\left(\frac{m_B V_M}{M_B S}\right)^2 \left(\frac{\Delta E_s}{\Delta E_\tau}\right)^2 \qquad (2)$$

Detailed definition for the parameters in the equation, including E_0, E_S, τ, t_0, $t_0+\tau$, E_τ, ΔE_S and $\Delta E\tau$ in GITT potential profiles is shown in Figure S11b.
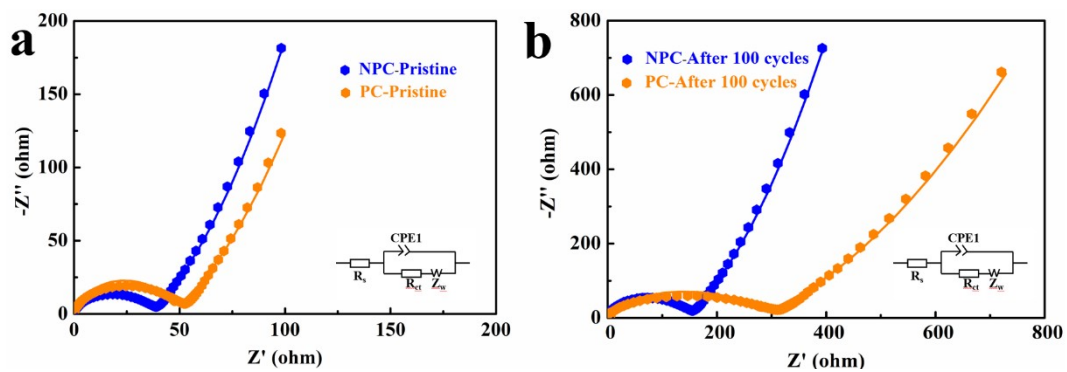
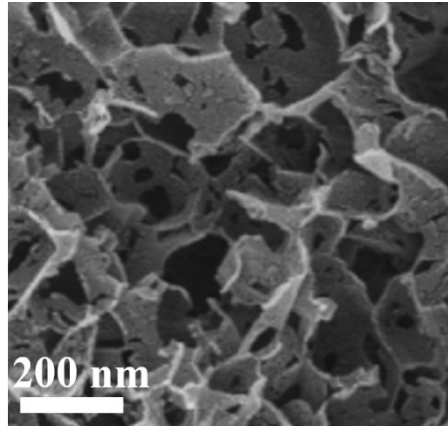**Figure S12.** Nyquist plots of EIS for NPC and PC. (a) Initial state and (b) after 100 cycles at a current density 1 A g^{-1}.
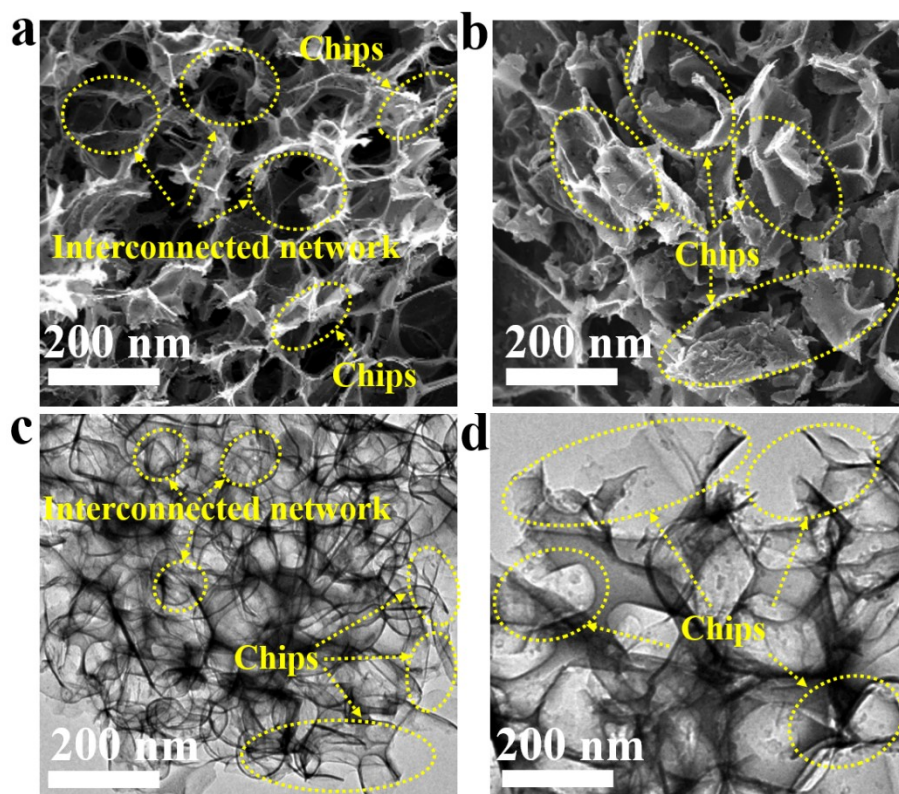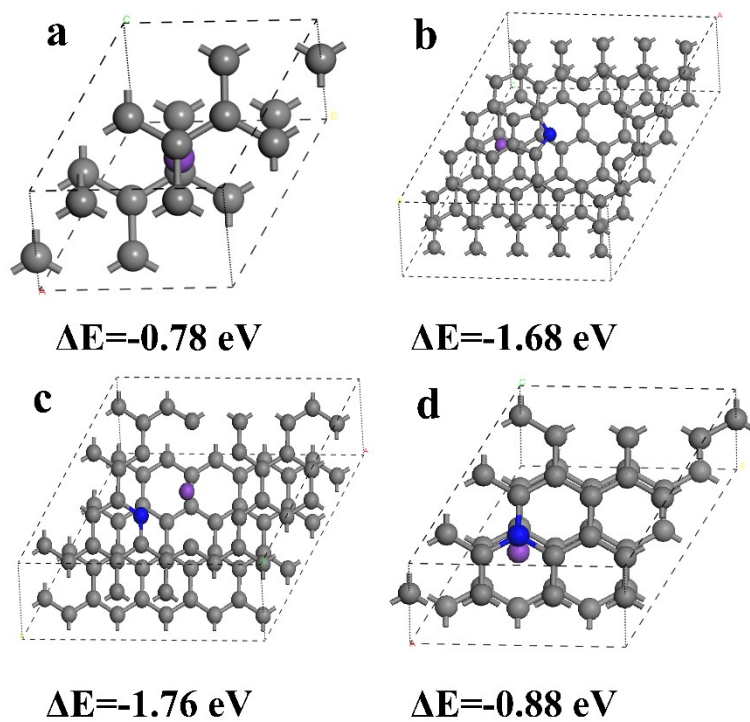
Figure S13. *Ex-situ* HRTEM images of NPC electrode after (a) fully discharged to 0.01 V and (b) fully charged to 2.5 V.

Figure S14. SEM image of NPC electrode over 1000 cycles at 1 A g^{-1}.

Figure S15. SEM and TEM images of NPC (a, c) and PC (b, d) electrodes after long cycle at 2 A g^{-1}, respectively.

a ΔE=-0.78 eV

b ΔE=-1.68 eV

c ΔE=-1.76 eV

d ΔE=-0.88 eV

Figure S16. The K-embedding energy for pristine carbon (a), N-5 (b), N-6 (c) and N-Q (d), respectively. Brown, blue and purple balls represent C, N and K atoms, respectively.
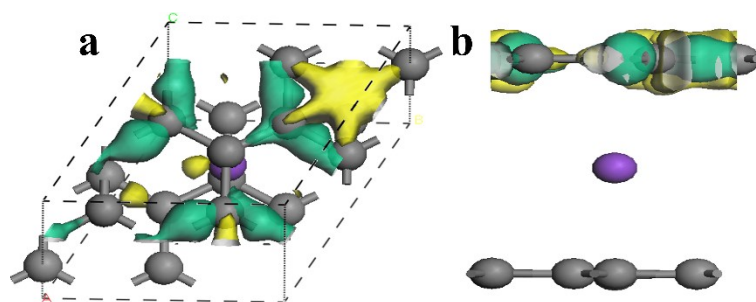
Figure S17. Top view (a) and side view (b) of electron density differences of K absorbed in the pristine

carbon.
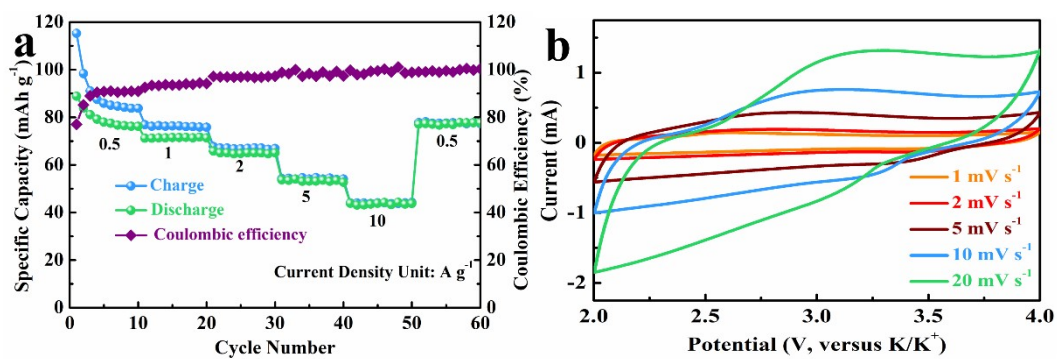
Figure S18. The electrochemical performance of AC. (a) Rate capability from 0.5 to 10 A g^{-1} and then to 0.5 A g^{-1}. (b) CV curves at different scan rates from 1 to 20 mV s^{-1}.
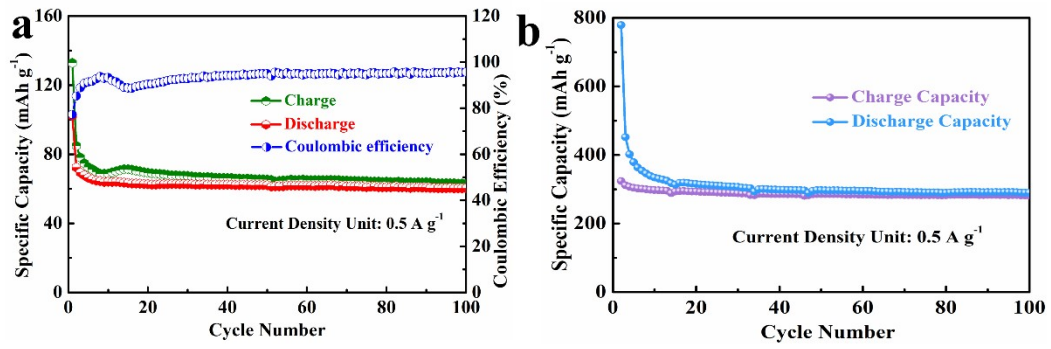
Figure S19. The cycle electrochemical performance over 100 cycles at 0.5 A g^{-1} for AC (a) and NPC (b), respectively.

Table S1. Comparison of carbon-based anodes in potassium-ion batteries

Material name	Cycled capacity (mAh g^{-1})/current density (mA g^{-1})	Cycle number	Ref.
NPC	171.2/2000	3000	This work
	257.7/500	500	
N/P-doped graphene	178/500	100	Ref. [2]
S-doped hollow carbon	316/100	100	Ref. [3]
Biomorphic N-doped carbon	236/200	200	Ref. [4]
Nitrogen-doped carbon	143/1000	2000	Ref. [5]
Hard carbon porous nanobelts	277/1000	1600	Ref. [6]
3D nitrogen-doped turbostratic carbon	200/1000	500	Ref. [7]
Nitrogen/sulfur co-doping carbon	105.2/2000	600	Ref. [8]
S/N co-doping graphene nanosheets	188.8/1000	2000	Ref. [9]
Nitrogen-doped soft carbon	165/1000	500	Ref. [10]
Nitrogen/phosphorus dual-doped porous carbons	153/1000	400	Ref. [11]
Sulfur-doped multichannel carbon fiber	150/1000	2000	Ref. [12]
Soft carbon nanofibers	48/2000	3000	Ref. [13]

Table S2. Electrical conductivity of AC cathode and NPC anode.

Site	Electrical conductivity (s cm^{-1})	
	AC cathode	NPC anode
Site 1	1.77812	1.33346
Site 2	1.77818	1.33344
Site 3	1.77815	1.33348
Average value	1.77815	1.33346

References

[1] Z. L. Jian, Z. Y. Xing, C. Bommier, Z. F. Li, X. L. Ji, Hard carbon microspheres: potassium-ion anode versus sodium-ion anode. Adv. Energy Mater. 6 (2016)1501874.

[2] W. Qiu, H. Xiao, Y. Li, X. Lu, Y. Tong, Nitrogen and phosphorus codoped vertical graphene/carbon cloth as a binder-free anode for flexible advanced potassium ion full batteries, Small 15 (2019) 1901285.

[3] J. Ding, H. Zhang, H. Zhou, J. Feng, X. Zheng, C. Zhong, E. Paek, W. Hu, D. Mitlin, Sulfur-grafted hollow carbon spheres for potassium-ion battery anodes, Adv. Mater. 31 (2019) 1900429.

[4] C. Gao, Q. Wang, S. Luo, Z. Wang, Y. Zhang, Y. Liu, A. Hao, R. Guo, High performance potassium-ion battery anode based on biomorphic N-doped darbon derived from walnut septum, J. Power Sources 415 (2019) 165-171.

[5] J. Li, Y. Li, X. Ma, K. Zhang, J. Hu, C. Yang, M. Liu, A honeycomb-like nitrogen-doped carbon as high-performance anode for potassium-ion batteries, Chem. Eng. J. 384 (2020) 123328.

[6] K. Zhang, Q. He, F. Xiong, J. Zhou, Y. Zhao, L. Mai, L. Zhang, Active sites enriched hard carbon porous nanobelts for stable and high-capacity potassium-ion storage, Nano Energy 77 (2020) 105018.

[7] W. Zhang, J. Yin, M. Sun, W. Wang, C. Chen, M. Altunkaya, A. Emwas, Y. Han, U. Schwingenschlögl, H. N. Alshareef, Direct pyrolysis of supermolecules: An ultrahigh edge-nitrogen doping strategy of carbonanodes for potassium-ion batteries, Adv. Mater. 32 (2020) 2000732.

[8] X. Shi, Y. Zhang, G. Xu, S. Guo, A. Pan, J. Zhou, S. Liang, Enlarged interlayer spacing and enhanced capacitive behavior of a carbon anode for superior potassium storage, Sci. Bull. 65 (2020) 2014-2021.

[9] W. Yang, J. Zhou, S. Wang, Z. Wang, F. Lv, W. Zhang, W. Zhang, Q. Sun, S. Guo, A three-dimensional carbon framework constructed by N/S co-doped graphene nanosheets with expanded interlayer spacing facilitates potassium ion storage, ACS Energy Lett. 5 (2020) 1653−1661.

[10] C. Liu, N. Xiao, H. Li, Q. Dong, Y. Wang, H. Li, S. Wang, X. Zhang, J. Qiu, Nitrogen-doped soft carbon frameworks built of well-interconnected nanocapsules enabling a superior potassium-ion batteries anode, Chem. Eng. J. 382 (2020) 121759.

[11] X. Ma, N. Xiao, J. Xiao, X. Song, H. Guo, Y. Wang, S. Zhao, Y. Zhong, J. Qiu, Nitrogen and phosphorus dual-doped porous carbons for high-rate potassium ion batteries, Carbon 179 (2021) 33-41.

[12] Y. Xu, J. Ruan, Y. Pang, H. Sun, C. Liang, H. Li, J.Yang, S. Zheng, Homologous strategy to construct high-performance coupling electrodes for advanced potassium-ion hybrid capacitors, Nano-Micro Lett. 13 (2021) 1-14.

[13] C. Zhang, Y. Xu, G. Du, Y. Wu, Y. Li, H. Zhao, U. Kaiser, Y. Lei, Oxygen-functionalized soft carbon nanofibers as high-performance cathode of K-ion hybrid capacitor, Nano Energy 72 (2020) 104661.